Surface redox chemistry of adsorbed viologens on Cu(100)

Duc-Thanh Pham,[a] Knud Gentz,[a] Caroline Zörlein,[a] Nguyen T. M. Hai,[a] Sung-Lin Tsay,[b] Barbara Kirchner,*[a] Simone Kossmann,[a] Klaus Wandelt[a] and Peter Broekmann*[a]

Received (in Montpellier, France) 3rd July 2006, Accepted 31st August 2006
First published as an Advance Article on the web 15th September 2006
DOI: 10.1039/b609421j

The surface redox-chemistry of adsorbed viologens is studied by means of cyclic voltammetry (CV) in combination with *in situ* scanning tunneling microscopy (STM). 1,1′-Dibenzyl-4,4′-bipyridinium molecules (DBV^{2+}) adsorb on a chloride modified Cu(100) electrode surface under formation of a laterally well ordered 2D array of supramolecular cavitand ensembles. Each cavitand consists at least of 4 individual DBV^{2+} sub-units which are arranged in a certain circular manner making this supramolecular cavitand chiral. Both possible enantiomeric forms are found in two mirror domains at the surface. Reducing the di-cationic $DBV^{2+}_{(ads)}$ species to the corresponding radical mono-cation $DBV^{\bullet+}_{(ads)}$ causes a phase transition from the pre-existing $DBV^{2+}_{(ads)}$ cavitand phase to a stripe pattern following a nucleation and growth mechanism. $DBV^{\bullet+}_{(ads)}$ species are adsorbed with their main molecular axis parallel to the surface in a side-on adsorption geometry. Enhanced intermolecular π–π-interactions are identified as the main driving force for the formation of 1D oligomer and polymer chains as the characteristic structural motif of the $DBV^{\bullet+}_{(ads)}$ phase. These structural motifs are generally independent of the electronic and structural substrate properties. Chloride desorption through the viologen film is discussed as the reason for an order–disorder transition within the viologen film at even more negative potentials.

1. Introduction

Nowadays, supramolecular chemistry has been well established as a major part of modern chemistry dealing with the design, fabrication and characterization of complex molecular architectures of nanometre sizes.[1–4] A particular challenge for supramolecular chemists is to provide artificial model systems allowing them to study the working principles of nano-sized devices, machines and actuators.[5] A successful strategy towards nano-scale molecular architectures is based on the so-called bottom-up approach. Here, supramolecular structures self-assemble from simpler molecular building-blocks *via* non-covalent weak forces which often reveal a directional character. As a result molecular architectures are obtained which exhibit a significantly higher complexity than the individual molecular building-blocks following Lehn's definition of supramolecular chemistry as the *"chemistry beyond the molecule"*.[1,2]

A promising approach to direct the ordering process of supramolecular architectures takes advantage of well defined surfaces of single crystals which can act as electronic and/or geometric templates due to the presence of specific adsorbate–substrate interactions. These are modulated according to the symmetry and periodicity of the substrate surface. Whereas in solution and in the 3D solid-state only the specific and directional intermolecular interactions govern the assembly of supramolecular architectures we find on surfaces, by contrast, a complex interplay of competing adsorbate–adsorbate and adsorbate–substrate interactions controlling the 2D phase behavior. Therefore, it does not astonish that structure motifs and intermolecular spacings of supramolecular ensembles are observed on surfaces which are known neither from the solution phase nor from the 3D solid-state.[6] The surface can be regarded as an effective template in the course of the 2D ordering of molecular building-blocks if enhanced adsorbate–substrate interactions are governing the 2D phase behavior.

However, surfaces are not only potential binding partners for these molecular building blocks. Furthermore, the surface can act as a reactant in terms of an electron-donor or electron-acceptor provided an electrochemical environment is used.

In this paper we present electrochemical and STM work on the adsorption behavior and surface redox-chemistry of viologens (1,1′-disubstituted-4,4′-bipyridinium molecules) that are adsorbed on an anion modified metal electrode surface (Fig. 1). Electrostatic interactions are supposed to play a crucial role for the immobilization of viologens, at least if chloride anions are pre-adsorbed on the electrode surface.

Viologens are certainly among the most intensively studied molecular building-blocks in supramolecular chemistry.[3] Their solution electrochemistry is well documented in the literature.[7,8] However, far less is known about the surface redox-chemistry and the related phase behavior of adsorbed viologens.

Certain attention was paid to the surface chemistry of viologens using standard electrochemical methods such as cyclic voltammetry (CV)[9,10] and various spectroscopic

[a] *Institute of Physical and Theoretical Chemistry, Bonn University, Wegelerstr. 12, 53115 Bonnn, Germany. E-mail: broekman@pc.uni-bonn.de; Kirchner@thch.uni-bonn.de; Fax: +49-(0)228-73-2515; Tel: +49-(0)228-73-3293*
[b] *Department of Physics, National Taiwan Normal University, 88, Ting-Chou Rd., Taipei, Taiwan*

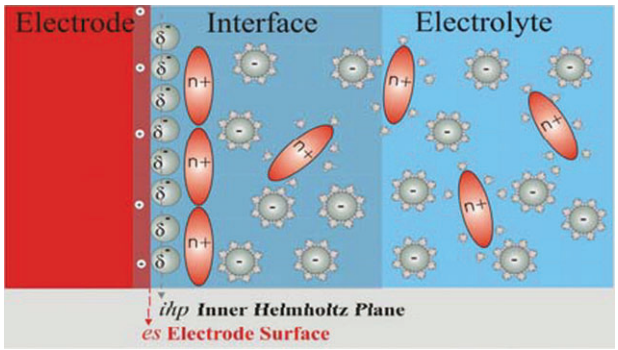

Fig. 1 Schematic drawing representing the structure of the solid/liquid interface in the presence of paired anion-cation layers. The redox-active cationic molecules are immobilized at the "inner Helmholtz plane" of specifically adsorbed chloride anions.

methods, *e.g.* Raman spectroscopy[11–15] or UV reflectance spectroscopy[16,17] in order to derive information about adsorption geometries depending on the particular redox-state. Characteristically, the reduction of pre-adsorbed viologen dications to the corresponding adsorbed radical mono-cation takes place at potentials more positive than the redox-processes of the corresponding solution species giving rise to the appearance of characteristic pre-peaks in the CV. Their appearance has been rationalized in terms of pure kinetic effects since reaction rates are usually higher for adsorbed reactants than for the corresponding solution species.[8] For the reaction of adsorbed species no diffusion limitations are expected. This phenomenon has been demonstrated for various viologens adsorbed on Hg[10,18,19] and HOPG[10,20,21] electrodes.

In the present paper we employ not only "integral" methods averaging over the entire surface but also scanning tunneling microscopy (STM) as a structure-sensitive local probe technique providing direct access to structural changes within adsorbed viologen films in the course of electron transfer reactions.

2. Experimental

STM results presented in this paper have been performed using a home-built electrochemical STM described in detail by Wilms *et al.*[22]

The tunneling tips used in our experiments were electrochemically etched from a 0.25 mm tungsten wire in 2 M KOH solution and subsequently coated by passing the tip through a film of hot-melt adhesive. For all solutions high purity water (Milli-Q purification system >18 MΩ cm, TOC <4 ppb) and reagent grade chemicals were used. All electrolyte solutions were degassed with oxygen-free argon for several hours before use. All potentials given in this paper are quoted *versus* the RHE. In order to guarantee a reproducibly smooth surface even after several electro-polishing procedures a surface orientation of less than 0.5° off the (100) plane was required (MaTeck company, Juelich, Germany). Prior to each STM experiment our copper sample had to be treated by an electrochemical etching procedure in order to remove the native oxide film. Therefore the surface was immersed into 50% orthophosphoric acid. Subsequently, an anodic potential of 2 V was applied between the copper electrode and a platinum foil for about 20 to 40 s.

Initial CV and STM measurements were routinely carried out in the pure supporting electrolyte (10 mM HCl). Such a pre-treatment of the copper surface in the chloride containing electrolyte appears advantageous since the high surface defect density originating from the initial electropolishing treatment is significantly reduced in the course of a so-called "electrochemical annealing" when chloride anions are specifically adsorbed.[22–24]

For the preparation of the redox-active viologen film on top of the anion-modified electrode surface the pure supporting electrolyte was routinely exchanged by a solution containing 10 mM HCl and 0.1 mM 1,1′-dibenzyl-4,4′-bipyridinium-dichloride in the potential regime between $E = +100$ mV and $E = -100$ mV.

3. Results and discussion

3.1 Structural features of the anion modified Cu(100) substrate

From the supporting electrolyte chloride anions specifically adsorb on Cu(100) forming a well ordered $c(2 \times 2)$-Cl phase[25–27] (Fig. 2) which is stable in the potential regime between the copper dissolution reaction and about $E = -300$ mV close to the onset of the HER (hydrogen evolution reaction). Fig. 2a–b show representative high-resolution STM images of the fourfold-symmetric chloride layer on top of a positively polarized Cu(100) electrode surface. The hard-sphere model of the resulting $c(2 \times 2)$-Cl phase is presented in Fig. 2c. In contrast to bromide and iodide, chloride anions remain to a large extent negatively charged upon adsorption.[28] Recent *in situ* XRD (X-ray diffraction) measurements could indeed evidence the ionic character of the Cu–Cl bond with an extraordinarily large Cu–Cl interlayer spacing of 1.88 Å and a resulting Cu–Cl bond length of 2.61 Å.[24] These characteristics make the chloride-modified Cu(100) electrode an interesting electronic and geometric template for the adsorption of positively charged organic molecules. Here, electrostatic interactions are assumed to play a crucial role for the immobilization of viologens at the so-called "inner Helmholtz plane" of specifically adsorbed chloride anions. In contrast, if iodide anions are pre-adsorbed, the attraction between the organic film and the substrate mainly originates from van der Waals type interactions.[29–31]

The presence of chloride on Cu(100) has impact not only on the atomic structure but also on the surface morphology on a mesoscopic length scale[26,27] originating from tremendous changes of the step and kink energies in the presence of the anion layer. Adsorbed chloride anions induce a preferential alignment of substrate steps parallel to the close packed chloride rows which are rotated by 45° with respect to the main symmetry axes of the underlying copper lattice (Fig. 2a). This morphological feature plays a major role in our experiments because it manifests the persistence of the $c(2 \times 2)$-Cl phase in the presence of the covering viologen film.

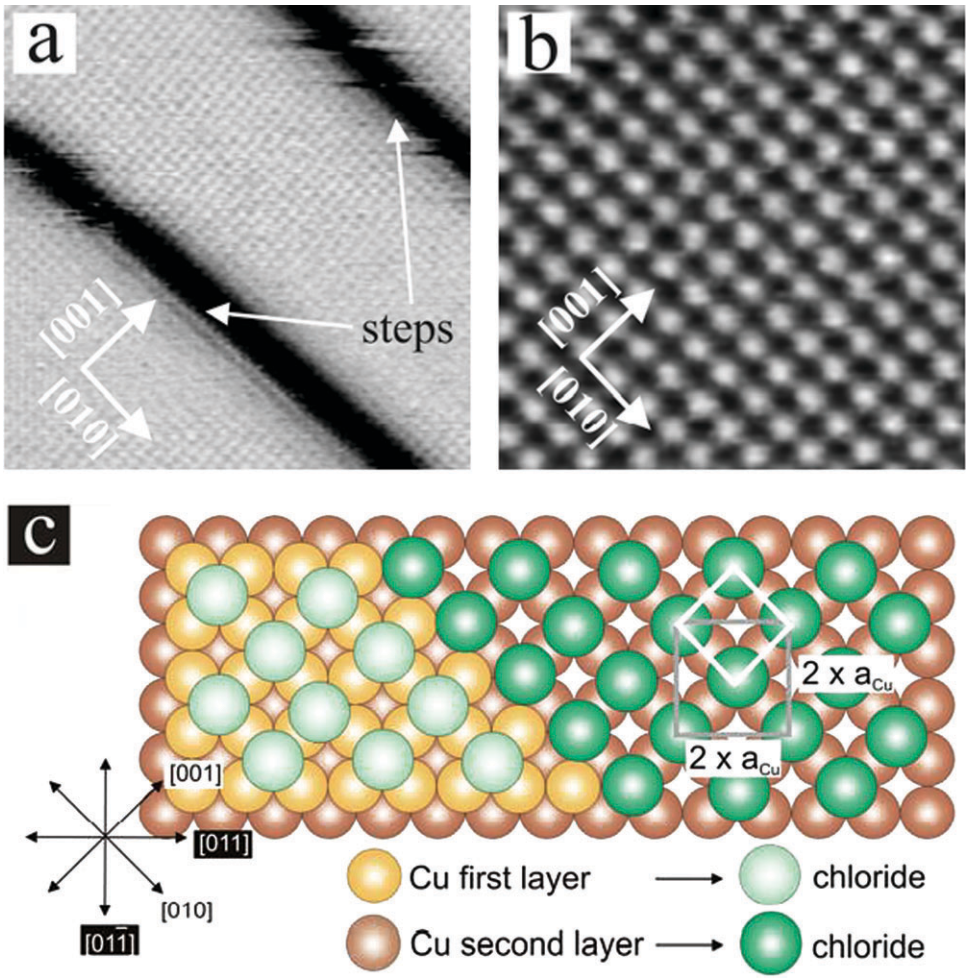

Fig. 2 Atomic structure and surface morphology of the chloride modified Cu(100) electrode surface, (a) Three substrate terraces are separated by two mono-atomically high steps which are aligned parallel to the [010]-direction; since this STM image is slightly differentiated the highest contrast is obtained at step edges, 13 nm × 13 nm, I_t = 5 nA, U_{bias} = −312 mV, E = −100 mV; (b) 4.2 nm × 4.2 nm, I_t = 0.67 nA, U_{bias} = 81 mV, E = −100 mV; (c) hard-sphere model of the $c(2 \times 2)$-Cl phase on Cu(100).

3.2 Structural features of the dibenzyl-viologen

For the quantum chemical optimization of the molecular viologen structures the density functional and *ab initio* programs provided by the TURBOMOLE 5.1 suite were used. The gradient corrected functional BP86 with the resolution of identity (RI) technique and the hybrid functional B3LYP were employed. The density functional theory (DFT) results are obtained from all-electron Kohn–Sham calculations. Ahlrichs' TZVP basis set is used throughout, featuring a valence triple-zeta basis set with polarization functions on all atoms.

Fig. 3 displays the result of the quantum chemical structure optimization obtained for the isolated di-cationic DBV^{2+}, the radical mono-cation $DBV^{\bullet+}$ and the uncharged DBV^0 species in the gas phase. As expected[7,8] the DBV^{2+} exhibits a pronounced non-zero interplanar dihedral-angle between the two pyridinium rings of $\Phi(DBV^{2+}) = 40.1°$, at least in the absence of any external forces. However, it is reported for the solution phase that counter ions with electron donor capabilities can undergo CT (charge transfer) interactions with viologen dications leading to a significant decrease of the dihedral angle Φ.[7,8] The same trend is observed for the reduction of the isolated DBV^{2+} to the corresponding radical mono-cation with a resulting dihedral angle $\Phi(DBV^{\bullet+}) = -5.4°$ (Fig. 3). For the uncharged DBV^0 molecule the dihedral angle is close to zero with $\Phi(DBV^0) = -0.1°$. These changes of the intramolecular structure become obvious from a side-view of the viologens along their main molecular axis (Fig. 3). A more detailed analysis of these changes of the intramolecular structure will be given in our forthcoming paper.[32]

All three common viologen redox-states can be converted into each other in an electrochemical environment by two single electron transfer reactions.[7,8] At least the first electron transfer process reducing the di-cation DBV^{2+} to the radical mono-cation $DBV^{\bullet+}$ is considered as reversible.[7,8]

3.3 Electrochemical characterization

Fig. 4 shows representative steady-state CVs of Cu(100) in the absence (black dotted curve) and the presence (grey curve) of viologen species.

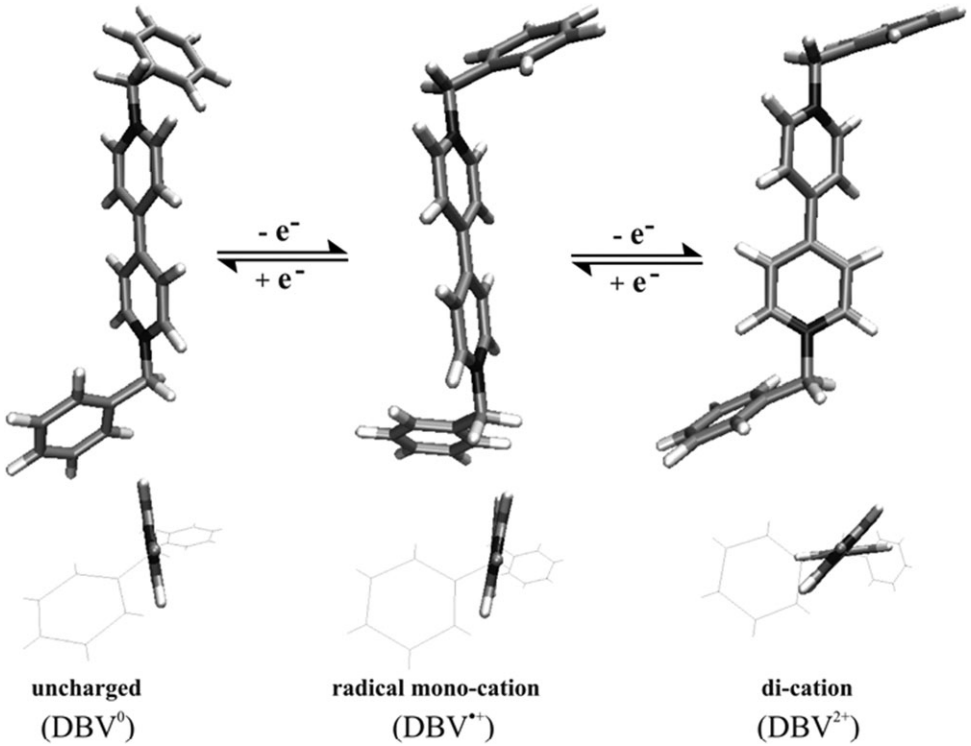

Fig. 3 DFT based structure optimization of the isolated DBV^{2+}, $DBV^{\bullet+}$ and the uncharged DBV^{0} molecules (for details see text).

The potential window of the Cu(100) electrode in the pure supporting electrolyte (10 mM HCl) is limited by two chemical reactions, the oxidative copper dissolution at the anodic limit and the reductive hydrogen evolution reaction (HER) at the cathodic limit. After exchanging the pure supporting electrolyte by the one containing the redox-active DBV^{2+} species we observe drastic changes in the CV curve. While the copper dissolution reaction remains almost unaffected by the presence of DBV^{2+} there is a considerable shift of the HER ($\Delta E \approx -140$ mV) towards lower potentials pointing to a pronounced inhibiting effect of viologens on the HER. Apparently, viologens are still present at the surface under these reductive conditions thereby blocking reactive sites for the HER such as substrate steps. A further deviation from the CV of the pure supporting electrolyte concerns the appearance of several anodic and cathodic current waves at potentials close to the HER regime. These additional current features have to be assigned to viologen-related redox processes. Typically, the shape of the CV in the presence of the viologen species depends strongly on the chosen cathodic potential limit.

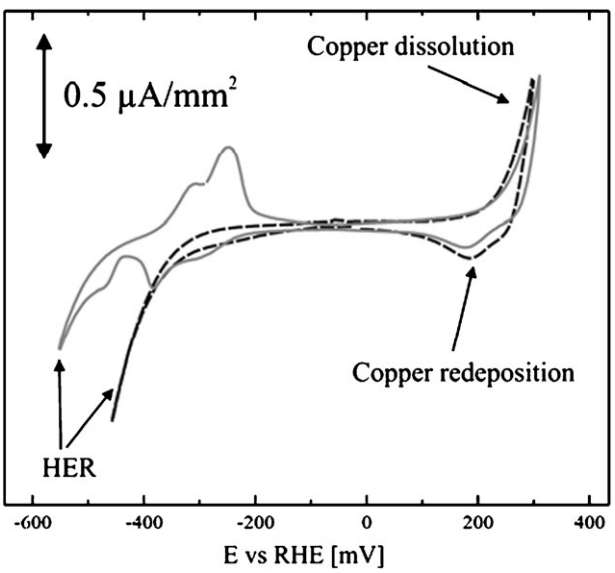

Fig. 4 Black dotted curve: CV of Cu(100) in the pure supporting electrolyte (10 mM HCl), $dE/dt = 10$ mV s^{-1}. Grey curve: CV of Cu(100) in the DBV^{2+} containing electrolyte (10 mM HCl, 0.1 mM $DBVCl_2$), $dE/dt = 10$ mV s^{-1}.

A precise correlation of the cathodic to the respective anodic current waves in the reverse potential scan is achieved by a systematic variation of the cathodic potential limit as shown in Fig. 5. By restricting the cathodic potential limit to $E = -330$ mV only the small peak pair P1/P′1 ($P1_{max} = -290$ mV, $P'1_{max} = -260$ mV) appears in the CV (CV 2 in Fig. 5). Extending the potential limit a bit further to $E = -410$ mV causes the appearance of P2/P′2 ($P2_{max} = -380$ mV, $P'2_{max} = -318$ mV, CV 4 in Fig. 5) revealing a slightly greater hysteresis of $\Delta E = 62$ mV than peak pair P1/P′1.

If the cathodic potential limit exceeds a critical value $E = -430$ mV we initiate not only the HER but also a further process related to the viologen redox-chemistry which is represented by P3/P′3. Characteristically the oxidation peak P′3 appears at similar potentials to P′1. P′3 increases in line

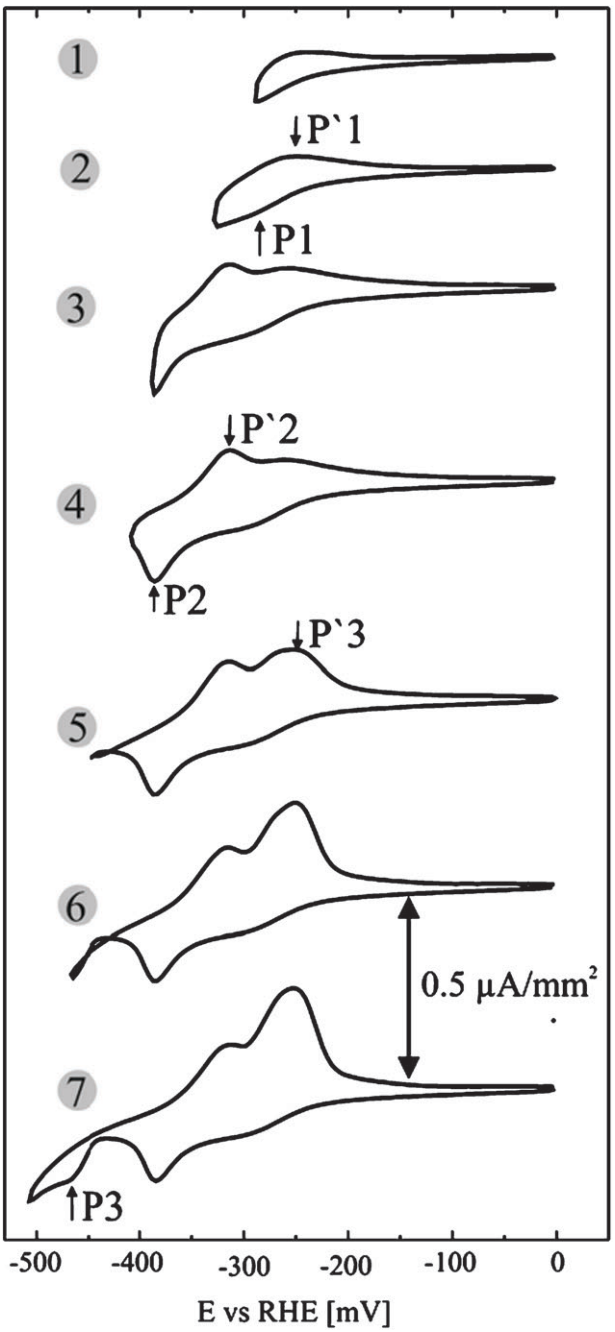

Fig. 5 Appearance of anodic and cathodic current waves in the CV of Cu(100) in the DBV^{2+} containing electrolyte (10 mM HCl, 0.1 mM $DBVCl_2$) upon changing the cathodic potential limit, dE/dt = 10 mV s^{-1}.

with the shift of the cathodic potential limit (CV 5–7 in Fig. 5). Besides the potential hysteresis there is also another remarkable difference between P1/P′1, P2/P′2 on the one hand and P3/P′3 on the other hand as demonstrated in Fig. 6. In this experiment the potential scan was stopped in the cathodic potential sweep at E = –425 mV after passing P1 and P2 (Fig. 6a) and at E = −475 mV at P3 (Fig. 6b), respectively. After a well defined hold-time at these potentials only the anodic potential scans were recorded. Obviously, there is no dependence of P′1 and P′2 on the potential hold time at E = −425 mV since all 4 curves (t_{hold} = 1–4 min) in Fig. 6a are identical. In contrast to that P′3 shows a strong dependence on the hold time at E = −475 mV (Fig. 6b). Peak height and the FWHM (full width at half maximum) increase with increasing hold time at E = −475 mV. Furthermore the peak maximum of P′3 is shifting towards higher potentials with increasing hold time.

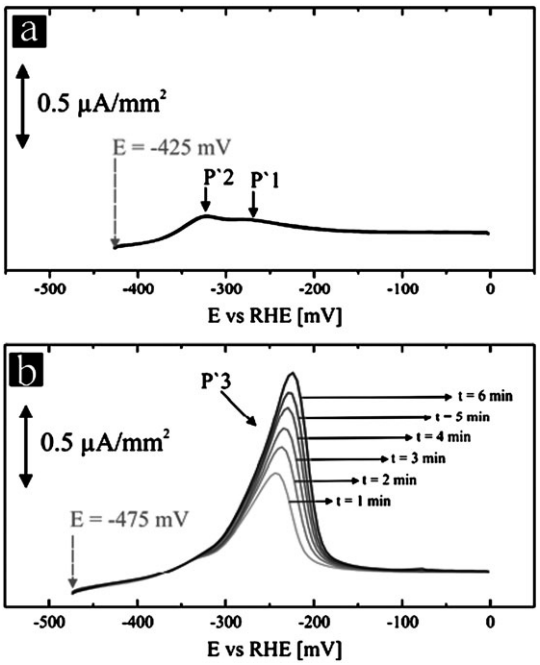

Fig. 6 (a) Set of four anodic potential sweep curves after holding the potential at E = −425 mV for 1, 2, 3 and 4 min, respectively (note, all four curves are identical!). (b) Set of six anodic potential sweep curves after holding the potential at E = −475 mV for 1 to 6 min, dE/dt = 10 mV s^{-1}.

We assign peak systems P1/P′1, P2/P′2 and P3/P′3 to the reduction of di-cationic DBV^{2+} to the corresponding radical mono-cationic $DBV^{\bullet+}$ species, related surface phase transitions and further precipitation/dissolution processes. The apparent complexity of this peak structure is due to the superposition of several processes involving "solution" as well as "surface limited" reactions:

1. The surface limited reduction/oxidation of pre-adsorbed viologen species according to

$$DBV^{2+}_{(ads)} + e^- \leftrightarrow DBV^{\bullet+}_{(ads)} \quad (1a)$$

which might be accompanied by the subsequent dimer formation[7,8] at the surface according to

$$2DBV^{\bullet+}_{(ads)} \leftrightarrow [DBV_2]^{2+}_{(ads)} \quad (1b)$$

or even an oligomer or polymer formation at the surface according to

$$nDBV^{\bullet+}_{(ads)} \leftrightarrow [DBV_n]^{n+}_{(ads)} \quad (1c)$$

2. The reduction/oxidation of viologen solution species according to

$$DBV^{2+}_{(aq)} + e^- \leftrightarrow DBV^{\bullet+}_{(aq)} \quad (2a)$$

which might be accompanied by the subsequent dimer formation in solution according to

$$2DBV^{\bullet+}_{(aq)} \leftrightarrow [DBV_2]^{2+}_{(aq)} \qquad (2b)$$

3. The film formation/dissolution of radical mono-cation chloride salts according to

$$n DBV^{\bullet+}_{(aq)} + n Cl^- \leftrightarrow [DBV^{\bullet+}Cl^-]_n \downarrow \qquad (3)$$

The further reduction of radical mono-cations to the fully uncharged viologen species is not considered here since this process is supposed to lie within the regime of massive hydrogen evolution at even more negative potentials. This can be deduced from the standard electrode potentials of $E^0(DBV^{2+}/DBV^{\bullet+}) = -330$ mV *vs.* RHE and $E^0(DBV^{\bullet+}/DBV^0) = -548$ mV *vs.* RHE for the first and the second electron transfer step, respectively.[8]

Recent experiments (not shown here) evidenced that at potentials below $E = -475$ mV a colored film appears at the surface, most likely due to the precipitation of the radical mono-cationic chloride salt (eqn (3)) as a consequence of massive reduction of $DBV^{2+}_{(aq)}$ solution species (eqn (2a)). Hence, P′3 might be associated with the oxidation of that film. These processes will be addressed in more detail in one of our forthcoming papers.[33]

In the following we focus on STM work dealing with specific structural changes within the pre-adsorbed viologen layer taking place upon reaching peak systems P1/P′1 and P2/P′2 in the CV.

3.4 Characterization by *in situ* STM

The exposure of a chloride-modified Cu(100) surface to the DBV^{2+} containing electrolyte within the double-layer potential regime leads instantaneously to the adsorption and subsequent lateral ordering of DBV^{2+} species at the surface. Since most structural features of the resulting $DBV^{2+}_{(ads)}$ phase were already presented by Safarowsky *et al.*[34,35] we discuss here only those results necessary for the understanding of the phase transition related to the electron transfer reaction. Surface morphology and molecular structure in the presence of $DBV^{2+}_{(ads)}$ are displayed in Fig. 7. Even after DBV^{2+} adsorption substrate steps are still aligned parallel to ⟨100⟩ directions (Fig. 7a). Obviously, the $DBV^{2+}_{(ads)}$ phase has no significant impact on the surface morphology which remains governed by the interaction of the specifically adsorbed chloride anions with the underlying copper lattice. The $DBV^{2+}_{(ads)}$ adlayer occurs in two mirror-domains denoted as I and II in Fig. 7a. On the molecular level this adlayer is composed of square-shaped molecular assemblies enclosing pronounced cavities in their center (Fig. 7b) with an apparent depth of about 0.38 nm and a typical width of 1.1 nm.[34] The structural relation of the $DBV^{2+}_{(ads)}$ adlayer to the chloride lattice underneath could be achieved by a careful variation of the tunneling conditions.[34,35] While under moderate tunneling conditions (high bias voltage, low tunneling current) the covering viologen film is imaged, the underlying chloride lattice becomes visible by applying more drastic tunneling conditions (low bias voltage, high tunneling current). In this latter case the tunneling tip penetrates into the organic film which leads to the local removal of viologens upon scanning. This kind of experiment suggests an interaction between the viologen film and the chloride lattice which is weaker than the chemisorptive Cu–Cl interaction. Note, the chemisorbed chloride layer cannot be removed by the tunneling tip.

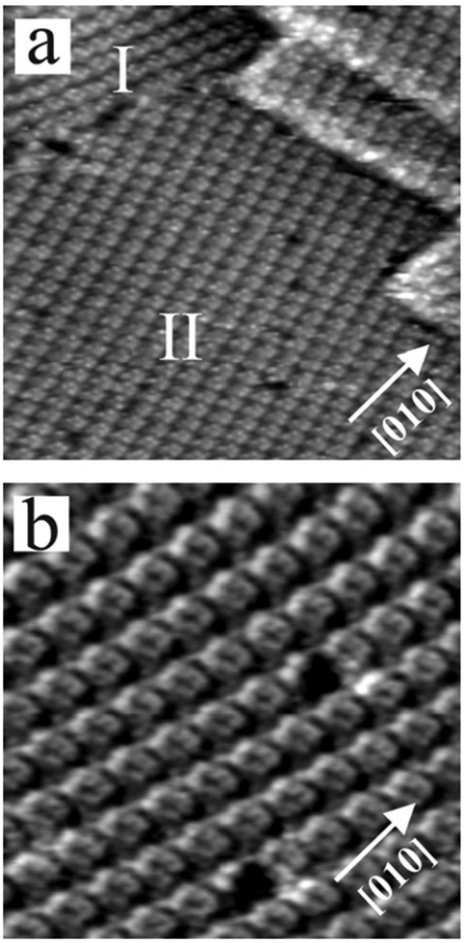

Fig. 7 Surface morphology and atomic structure of Cu(100) in the presence of $DBV^{2+}_{(ads)}$, (a) 52 nm × 52 nm, $I_t = 0.1$ nA, $U_{bias} = 46$ mV, $E = +25$ mV; (b) 24 nm × 24 nm, $I_t = 0.1$ nA, $U_{bias} = 46$ mV, $E = +25$ mV.

A graphical superposition of two STM images showing the cavitand structure of the $DBV^{2+}_{(ads)}$ film and the chloride lattice underneath is presented in Fig. 8a.[35] With the $c(2 \times 2)$-Cl phase serving as internal calibration lattice we could describe the $DBV^{2+}_{(ads)}$ unit cell either by a $\begin{vmatrix} 2 & 7 \\ \overline{7} & 2 \end{vmatrix}$ transformation matrix or in Wood notation by a $(\sqrt{53} \times \sqrt{53})R15.9°$ unit-mesh with lattice constants of $|\vec{a}| = |\vec{b}| = 2.6$ nm ± 0.02 nm enclosing an angle of 90° ± 2° (see model in Fig. 8c). Alternatively, the two-dimensional $DBV^{2+}_{(ads)}$ array could be directly related to the copper substrate assuming a $(\sqrt{106} \times \sqrt{106})R29.05°$ unit-mesh or a $\begin{vmatrix} 5 & 9 \\ \overline{9} & 5 \end{vmatrix}$-matrix transforming the Cu(100)–(1×1) lattice into the unit-cell of the $DBV^{2+}_{(ads)}$ adlayer. An individual cavitand seems to consist of four rod-shaped subunits (Fig. 8b). In our preliminary structure model[34,35] these are assigned to four individual bipyridinium cores of $DBV^{2+}_{(ads)}$ molecules. Individual bipyridinium cores within the cavitand are roughly

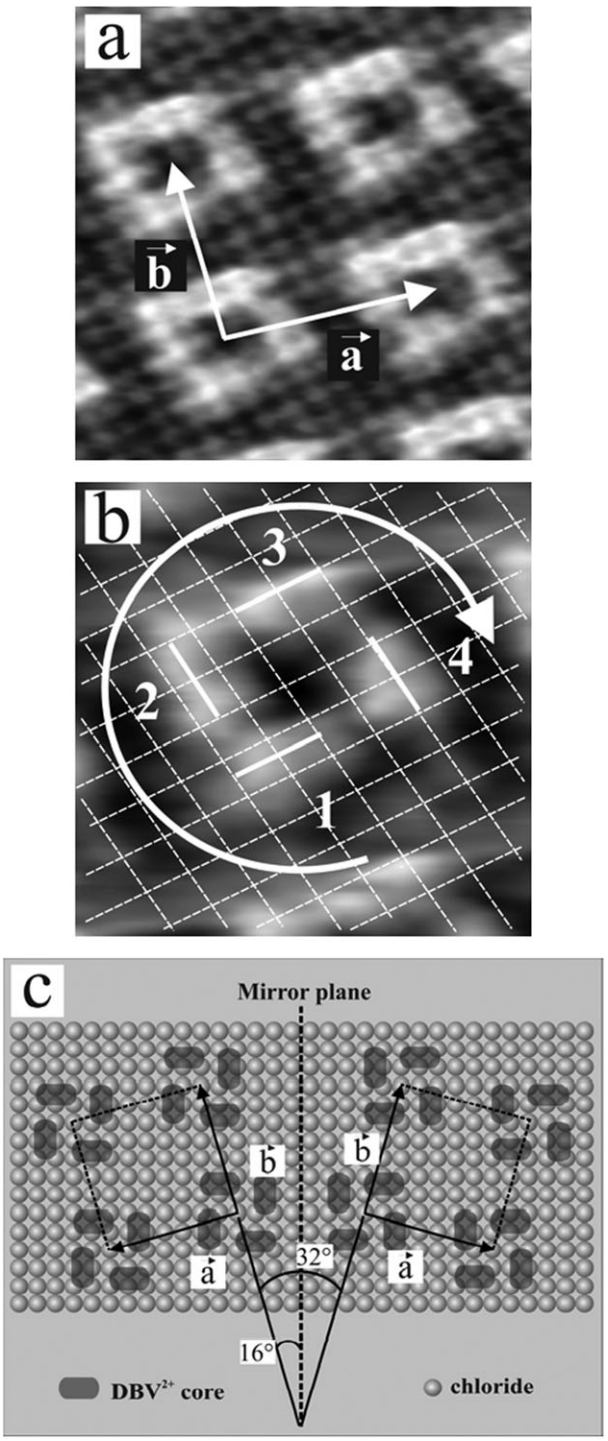

Fig. 8 (a) Transparent superposition of the atomically resolved chloride lattice with the $DBV^{2+}_{(ads)}$ adlayer (for details see text), 5.6 nm × 5.6 nm; (b) circular chirality of the $DBV^{2+}_{(ads)}$ cavitand ensemble indicated by the white arrow; the white grid represents the chloride lattice, 3.1 nm × 3.1 nm, I_t = 0.25 nA, U_{bias} = 86 mV, E = +50 mV; (c) tentative structure model of the $DBV^{2+}_{(ads)}$ cavitand phase reflecting the STM imaging contrast.

aligned parallel to the close packed chloride rows underneath (Fig. 8b). From crystalline chloride salts of viologens it is known that bipyridinium cores are coordinated by chloride counter ions directly either above or below the nitrogen atoms.[8] A similar coordination of the $DBV^{2+}_{(ads)}$ species appears plausible on the Cu(100)–$c(2 \times 2)$-Cl phase since the N–N distance of 7.1 Å within the DBV^{2+} molecule agrees well with the double Cl–Cl spacing along the ⟨100⟩ substrate directions of 7.2 Å. However, it should be noted that "absolute" adsorption geometries cannot be derived only on the basis of STM data. Therefore, this adsorption model remains tentative and needs to be confirmed by complementing techniques sensitive to adsorption geometries, *e.g. in situ* IR.

Due to the circular arrangement of these four subunits individual cavitands are chiral (Fig. 8b). For symmetry reasons one would expect both enantiomeric forms to be present on the achiral surface. Indeed, both enantiomers are observed in the two mirror domains of the $DBV^{2+}_{(ads)}$ adlayer (see also Fig. 11).[35]

The particular cavitand structure of the $DBV^{2+}_{(ads)}$ species on the chloride modified Cu(100) is the result of the complex interplay between competing adsorbate–substrate and adsorbate–adsorbate interactions. The presence of the negatively charged chloride lattice is needed in order to increase the $DBV^{2+}_{(ads)}$ surface concentration most likely by attractive electrostatic interactions. The lateral mobility of $DBV^{2+}_{(ads)}$ molecules on Cu(100)–$c(2 \times 2)$-Cl right after adsorption is still high enough to allow fast 2D ordering resulting in laterally extended domains of the $DBV^{2+}_{(ads)}$ cavitand structure. The crucial role of the chloride can be deduced from recent STM experiments on the DBV^{2+} adsorption on bromide modified Cu(100) (Fig. 9). Similar to chloride also bromide anions form a $c(2 \times 2)$ adlattice on Cu(100).[36] However, the charge transfer upon adsorption is much more efficient for bromide than for chloride[28] resulting in an almost discharged bromide layer on Cu(100) with a pronounced covalent nature of the Cu–Br bond. According to that we expect a reduced attraction of the $DBV^{2+}_{(ads)}$ species by the bromide lattice. Indeed, no full monolayer of $DBV^{2+}_{(ads)}$ species could be obtained on Cu(100)–$c(2 \times 2)$-Br under similar experimental conditions (Fig. 9a) since the $DBV^{2+}_{(ads)}$ surface concentration on $c(2 \times 2)$-Br was not sufficient for the completion of the 2D condensation. In this submonolayer regime the local ordering of the $DBV^{2+}_{(ads)}$ species, however, is identical to what we have found on Cu(100)–$c(2 \times 2)$-Cl. Local patches of the $(\sqrt{53} \times \sqrt{53})$ R15.9°–$DBV^{2+}_{(ads)}$ cavitand superstructure are clearly observed on bromide modified Cu(100) (Fig. 9).

Obviously, it is the substrate symmetry with identical interhalide spacings that strongly influences the lateral ordering of the $DBV^{2+}_{(ads)}$ species while the electronic substrate properties (*e.g.* the remaining charge on the halide upon adsorption) are crucial for the precedent adsorption process from solution. By changing substrate symmetry, *e.g.* by using a pseudo-hexagonal Cu(111)–$c(p \times \sqrt{3})$-Cl phase as substrate, we obtain again a full monolayer of $DBV^{2+}_{(ads)}$ species which, however, reveals different structure motifs from those found on the square Cu(100)–$c(2 \times 2)$-Cl phase.

On HOPG (highly oriented pyrolytic graphite), by contrast, anions do not specifically adsorb so that the $DBV^{2+}_{(ads)}$ molecules interact directly with the graphite electrode surface. It is the extremely weak interaction of the HOPG surface with the $DBV^{2+}_{(ads)}$ species at positive potentials in combination with the repulsive electrostatic interactions between positively charged

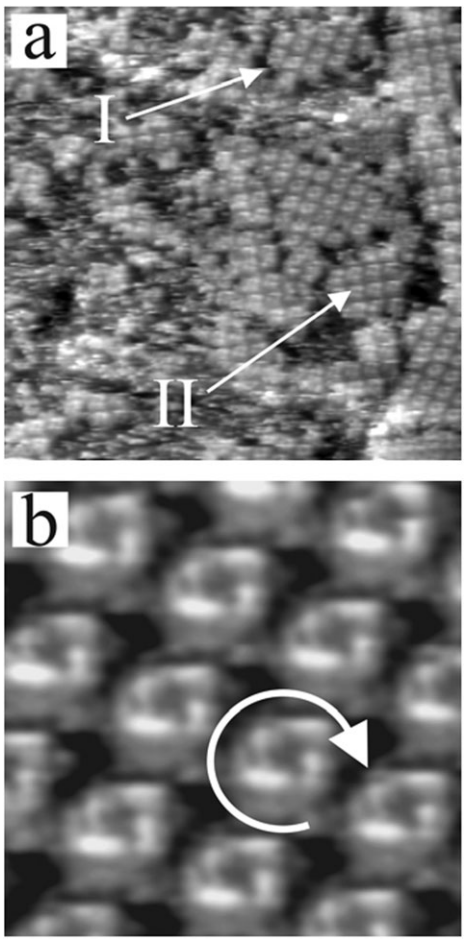

Fig. 9 $DBV^{2+}_{(ads)}$ submonolayer on the Cu(100)–$c(2 \times 2)$-Br phase, (a) 56 nm × 56 nm, $I_t = 0.1$ nA, $U_{bias} = -276$ mV, $E = +117$ mV, the white arrows indicate the presence of two mirror domains of the $DBV^{2+}_{(ads)}$ cavitand structure; (b) 8.4 nm × 8.4 nm, $I_t = 0.1$ nA, $U_{bias} = -278$ mV, $E = +117$ mV.

$DBV^{2+}_{(ads)}$ species that prevents lateral ordering of $DBV^{2+}_{(ads)}$ on HOPG.[33]

The $DBV^{2+}_{(ads)}$ related cavitand structure on Cu(100)–$c(2 \times 2)$-Cl is stable only down to potentials of about −240 mV. Reaching the potential regime where P1 appears in the CV (Fig. 5–6) we initiate the reduction of the viologen di-cation to the corresponding radical mono-cation which leads to a slow decay of the $DBV^{2+}_{(ads)}$ cavitand phase as demonstrated in Fig. 10. This process is accompanied by the nucleation and subsequent growth of a new stripe pattern phase that occurs in two mirror and two further rotational domains (Fig. 10f).

Defects such as translational or mirror domain boundaries within the pre-existing $DBV^{2+}_{(ads)}$ cavitand phase serve as preferential nucleation centers for this growth process (see white circles in Fig. 10a and b). Due to the slow transition kinetics there is a wide potential range of co-existence of both phases in the cathodic potential sweep ranging from $E = -240$ mV to $E = -320$ mV. The phase transition is fully completed at about $E = -330$ mV.

Fig. 11 shows a molecularly resolved STM image obtained in this coexistence potential regime with isolated $DBV^{2+}_{(ads)}$ cavitands surrounded by short chains of the stripe pattern. Their lateral order and structural relation to the substrate is still poor in this intermediate regime. Ongoing ripening processes after the initial nucleation and growth lead to an overall improvement of the lateral order of this stripe pattern, the increase of domain sizes and to a significant decrease of the domain boundary density indicating that the presence of these domain boundaries is energetically unfavorable. Such a local ripening phenomenon is presented in the series of STM images in Fig. 12 showing the rapid decay of a smaller domain (denoted as I) of the stripe pattern that is embedded in its corresponding mirror domain (denoted as II). Individual stripes seem to be cross-linked close to the mirror domain boundary (indicated by the white arrows in Fig. 12a) leading to a "honeycomb" like appearance of the stripe pattern in proximity to the domain boundary. High resolution STM images (not shown here) indicate that this honeycomb-like appearance results from a meandering of stripes caused by an enhanced mobility of individual viologen molecules at defect sites such as domain boundaries. After completion of these ripening processes individual domains of the stripe pattern often extend over entire substrate terraces, see *e.g.* terraces T1, T2 and T3 in Fig. 13a.

In principle, the transition of the $DBV^{2+}_{(ads)}$ cavitand to the stripe pattern phase can be regarded as a quasi-reversible process. Sweeping the potential back towards the double layer regime converts the stripe pattern back into the $DBV^{2+}_{(ads)}$ cavitand phase (Fig. 13). This transition preferentially starts again at defect sites, *e.g.* at mono-atomically high substrate steps which serve as natural domain boundaries of the stripe pattern. Comparing Fig. 13a and f it becomes evident that the appearance of both mirror domains of the $DBV^{2+}_{(ads)}$ cavitand phase is independent of the pre-orientation of the stripe pattern. Both mirror domains of the $DBV^{2+}_{(ads)}$ cavitand phase can originate from the same mirror domain of the stripe pattern.

The surface morphology after completion of the reduction of $DBV^{2+}_{(ads)}$ to $DBV^{\bullet+}$ is still dominated by substrate steps that are parallel to the ⟨100⟩ directions (Fig. 14). Since the surface morphology remains largely unaffected by this phase transition we definitely rule out a chloride desorption/re-adsorption as the origin of these phase transitions. Substrate steps would immediately lose their orientation parallel to the ⟨100⟩ directions when the $c(2 \times 2)$-Cl phase disappears in the course of chloride desorption.[26,27] Note that in the pure supporting electrolyte chloride desorption already starts in the potential regime between $E = -290$ mV and $E = -320$ mV. The presence of the viologen adlayer obviously causes not only a downward shift of the HER onset potential. The same trend is also observed for the chloride desorption. The presence of the viologen adlayer apparently gives rise to an additional increase of the activation barrier for the chloride desorption. From these results it becomes evident that the electron transfer from the metal to the redox-active species occurs through the "inner Helmholtz plane" of specifically adsorbed chloride anions (Fig. 1).

Since we change the delicate balance between the substrate–adsorbate and the adsorbate–adsorbate interactions by the electron transfer a resulting change in the lateral ordering within the viologen film appears plausible. For the

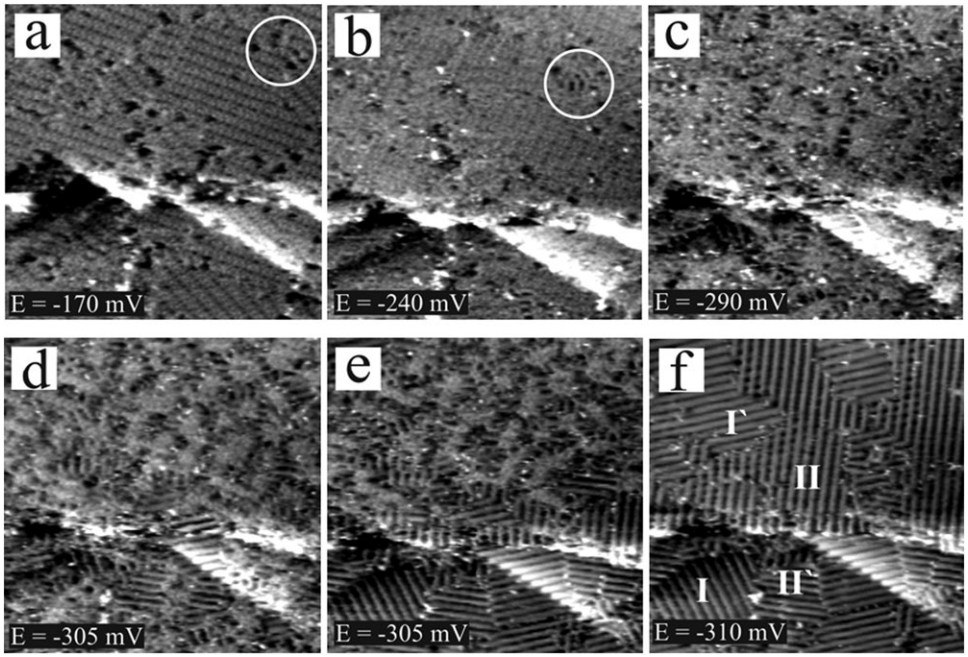

Fig. 10 Series of STM images showing the surface phase transition upon reduction of the $DBV^{2+}_{(ads)}$ to the corresponding $DBV^{\bullet+}_{(ads)}$ species, (a–f) 54 nm × 54 nm, I_t = 0.1 nA, U_{bias} = 200 mV. The appearance of four domains of the stripe pattern in Fig. 10f can be explained in terms of two mirror domains and a further two rotational domains. Apparently, the propagation directions of the stripe pattern are not aligned with any main symmetry direction of the chloride lattice underneath.

resulting $DBV^{\bullet+}_{(ads)}$ film we expect both reduced repulsive electrostatic interactions due to the reduced positive charge on the adsorbed viologens and increased intramolecular interactions. From the solution phase chemistry of viologens it is known[8,9] that the paramagnetic radical mono-cations reveal a strong tendency towards dimerization in particular in an aqueous environment resulting in highly soluble and spin-paired $[DBV_2]^{2+}_{(aq)}$ species (see eqn (2b)). Driving forces for such a spontaneous dimerization in solution are enhanced π–π interactions between bipyridinium cores and the tendency towards spin-pairing in the reduced redox state which can even overcompensate the repulsive electrostatic interactions between those radical mono-cations.[8] The standard Gibbs' free energy for the exergonic dimerization of $DBV^{\bullet+}_{(aq)}$ species in an aqueous and chloride containing solution amounts to $\Delta G^0 = -16.81$ kJ mol^{-1}.[8]

Blandamer *et al.* even report an oligomerization of di-alkylated radical mono-cations in solution.[8,37]

A similar tendency towards oligomerization and polymerization is observed here on the electrode surface (Fig. 10 and 11). The observed stripe pattern formation can be understood in terms of the 2D ordering of the adsorbed $DBV^{\bullet+}_{(ads)}$ species into 1D oligomer and polymer aggregates $[DBV_n]^{n+}_{(ads)}$ according to eqn (1c). Here, "polymerization" does not imply a covalent bonding as it has been reported for a $DBV^{\bullet+}$ polymer being irreversibly formed by a "prolonged electrolysis of an aqueous solution".[8,38,39] The stripe pattern phase on Cu(100)–$c(2 \times 2)$-Cl can be quasi-reversibly transformed back into the $DBV^{2+}_{(ads)}$ cavitand phase by applying potentials in the double layer regime as evidenced in Fig. 13. While the first electron transfer step in the viologen redox-chemistry of solution species is often considered as a fast and fully reversible process[7,8] the related surface phase transitions of the adsorbed viologen species are slow and therefore reveal a considerable potential hysteresis which arises from additional activation barriers. These might originate from the required positional and conformational changes of viologen molecules within the condensed 2D layer in the course of the phase transition. Note, the restoration of the $DBV^{2+}_{(ads)}$ cavitand phase in the anodic potential sweep is completed only at E = 0 mV (Fig. 13). In particular the transition from the stripe pattern to the $DBV^{2+}_{(ads)}$ cavitand phase seems to be kinetically hindered. Such a kinetic hindrance appears plausible considering that intermolecular π–π-bonds have to be broken upon this phase transition.

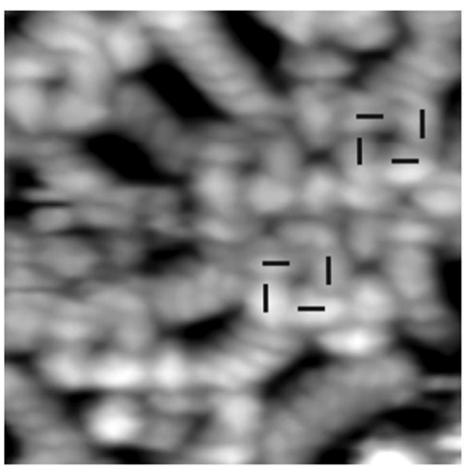

Fig. 11 Coexistence of $DBV^{\bullet+}_{(ads)}$ and $DBV^{2+}_{(ads)}$ species at the surface, 8.5 nm × 8.5 nm, I_t = 0.38 nA, U_{bias} = 161 mV, E = −315 mV.

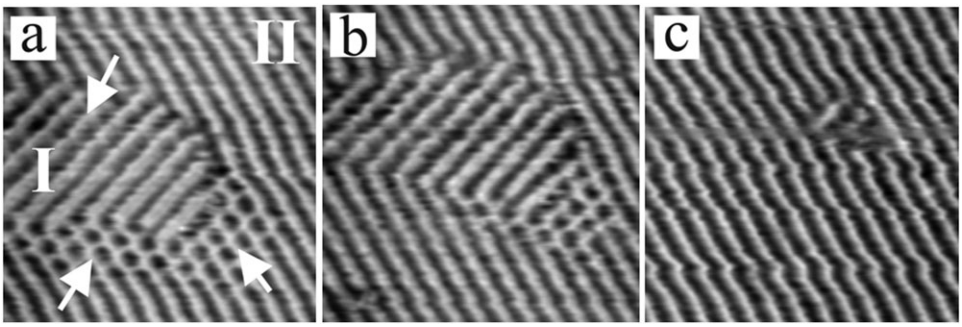

Fig. 12 Time resolved ripening processes within the stripe pattern phase, (a–c) 24 nm × 24 nm, I_t = 0.1 nA, U_{bias} = 134 mV, E = −320 mV.

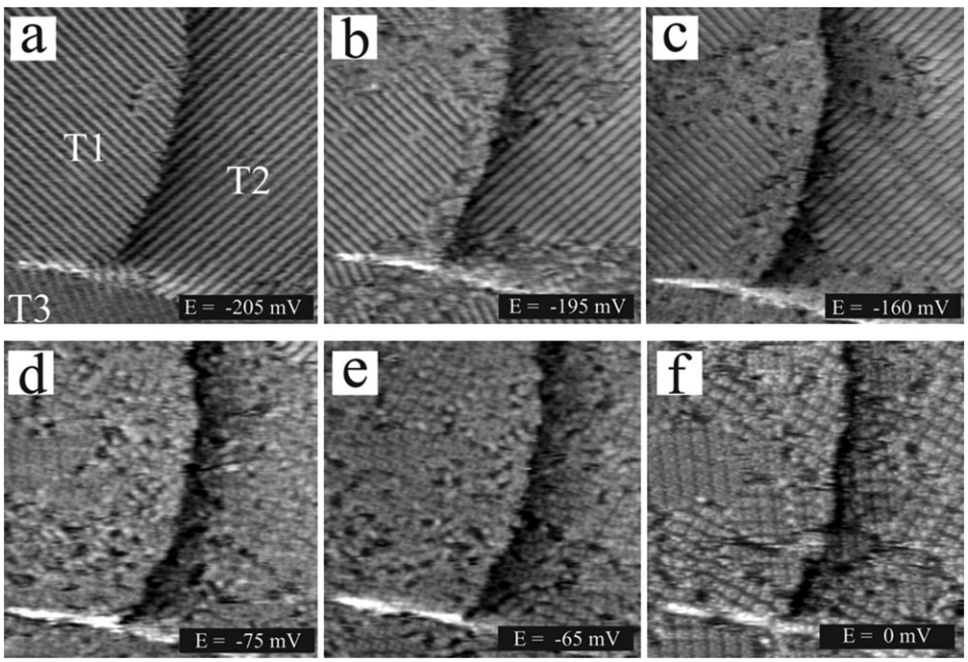

Fig. 13 Series of STM images showing the decay of the stripe pattern phase and the subsequent growth of the $DBV^{2+}_{(ads)}$ cavitand structure upon increasing potentials, (a–f) 53.2 nm × 53.2 nm, I_t = 0.15 nA, U_{bias}: ranging from 228 mV to 310 mV.

Individual $DBV^{\bullet+}_{(ads)}$ molecules within the $[DBV_n]^{n+}_{(ads)}$ oligomer and polymer chains are often imaged as elongated "discs" (Fig. 11, 15a and 16) with an intermolecular spacing of 3.6 ± 0.2 Å within and 1.82 nm between adjacent $[DBV_n]^{n+}_{(ads)}$ chains (Fig. 15a). However, the particular imaging contrast is very sensitive to the applied tunneling conditions. A selective imaging of the more conductive bipyridinium redox-centers is obtained in Fig. 15b.

The structural correlation to the chloride lattice is achieved by the local removal of the viologen layer upon scanning under drastic tunneling conditions (Fig. 15c).

For the stripe pattern phase we propose in Fig. 16 a tentative structure model of only one possible mirror domains with individual $DBV^{\bullet+}_{(ads)}$ molecules residing with their main molecular axes parallel to the surface in a side-on adsorption geometry. The stripe propagation direction encloses a characteristic angle of α = 37° with one of the main symmetry axes of the chloride lattice. The bright stripes in Fig. 15a–b are assigned to bipyridinium cores arranged in an almost face-to-

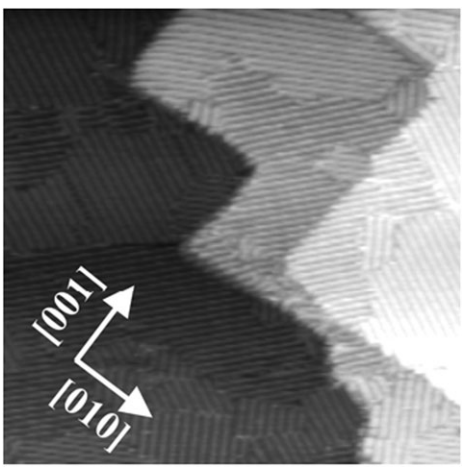

Fig. 14 Surface morphology of Cu(100) in the presence of the stripe pattern phase on Cu(100)–$c(2 \times 2)$-Cl, 87 nm × 87 nm, I_t = 0.4 nA, U_{bias} = 167 mV, E = −321 mV.

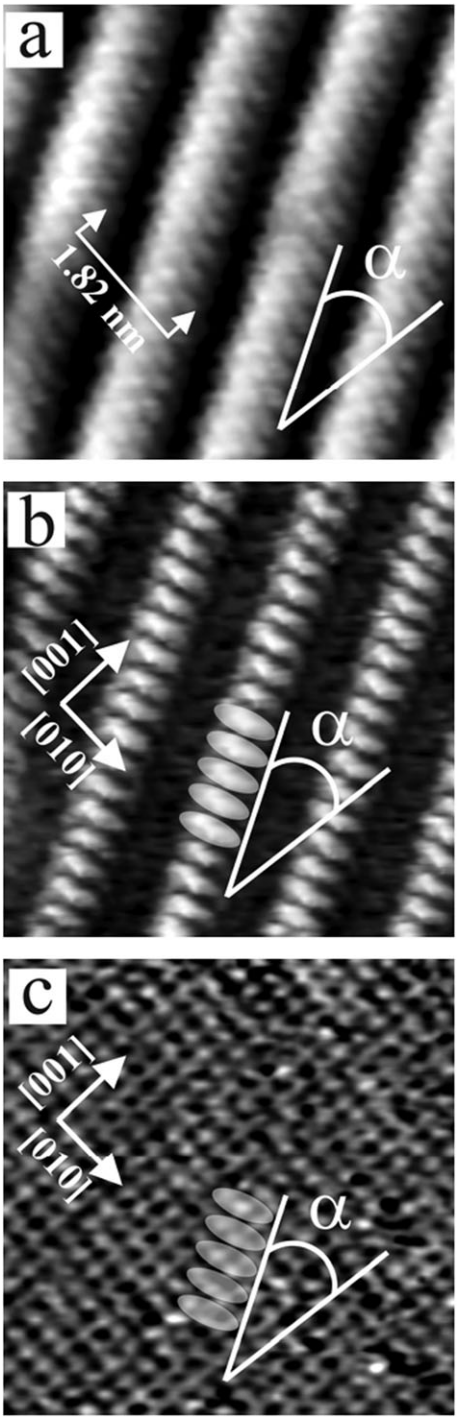

Fig. 15 Structural correlation between the stripe pattern phase and the Cu(100)–$c(2 \times 2)$-Cl lattice underneath by a systematic variation of the tunneling conditions, (a) 6.8 nm × 6.8 nm, I_t = 4 nA, U_{bias} = 93 mV, E = −200 mV (cathodic potential sweep); (b) 6.8 nm × 6.8 nm, I_t = 4 nA, U_{bias} = 28 mV, E = −200 mV (cathodic potential sweep); (c) 6.8 nm × 6.8 nm, I_t = 9 nA, U_{bias} = 1 mV, E = −130 mV (cathodic potential sweep).

face orientation. Benzyl groups are expected to lie within the dark troughs revealing a reduced STM imaging contrast. Essential for the formation of such a 1D polymer chain with a nearest neighbor distance of only 3.6 ± 0.2 Å is the almost

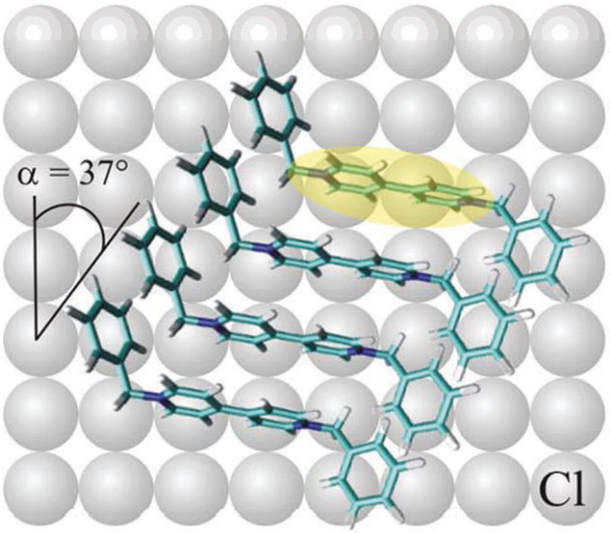

Fig. 16 Tentative structure model of one possible mirror domain of the stripe pattern phase on Cu(100)–$c(2 \times 2)$-Cl based on the STM data shown in Fig. 15b–c.

planar conformation of the bipyridinium cores in the reduced state (Fig. 3). A dihedral angle of Φ = 40.1° as predicted for the DBV^{2+} species (Fig. 3) would not allow such a small

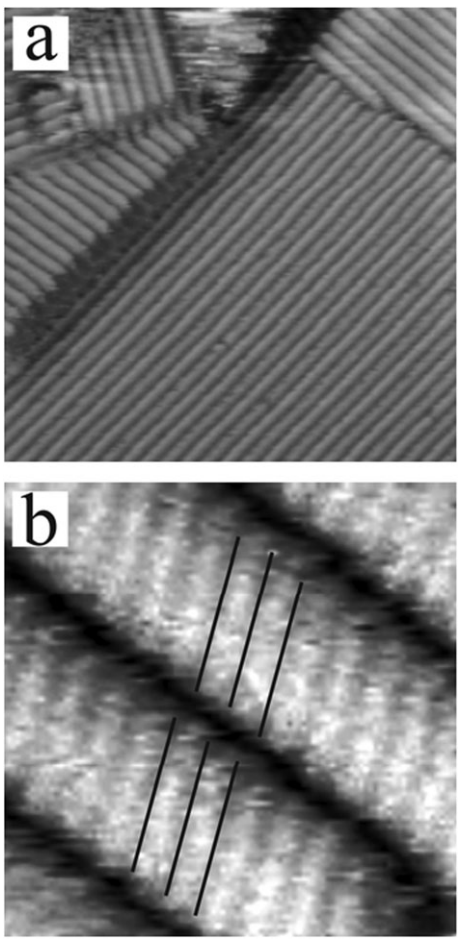

Fig. 17 Stripe pattern phase obtained on HOPG, (a) 45 nm × 45 nm, I_t = 0.2 nA, U_{bias} = +337 mV, E = −272 mV; (b) 3.8 nm × 3.8 nm, I_t = 0.2 nA, U_{bias} = +337 mV, E = −380 mV.

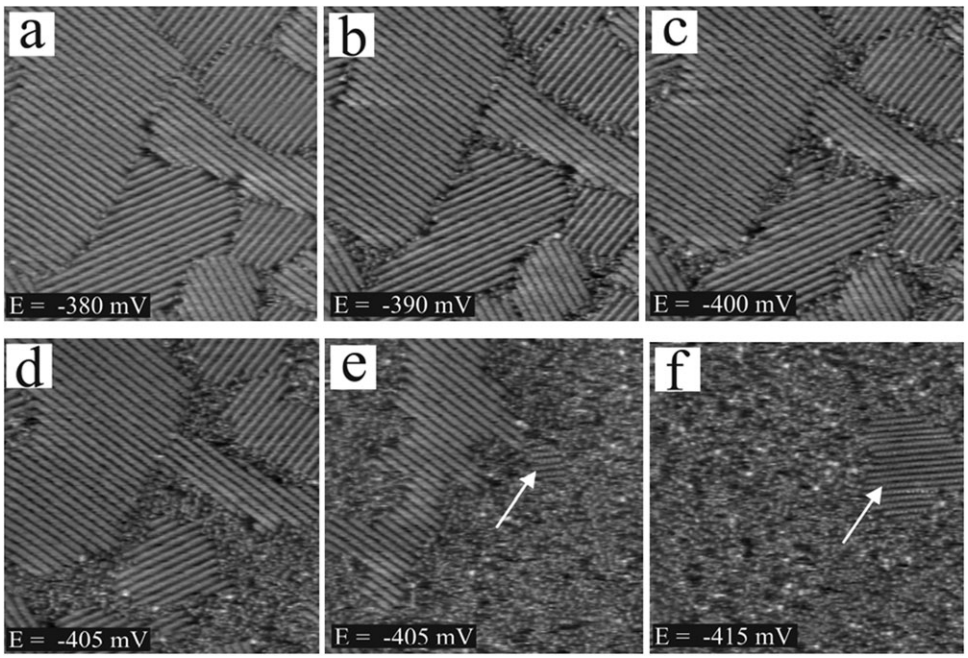

Fig. 18 Decay of the stripe pattern phase due to chloride desorption upon reaching the potential regime where P2 appears in the CV, (a–f) 57.6 nm × 57.6 nm, I_t = 0.2 nA, U_{bias} = 268 mV.

intermolecular distance within the 1D polymer chain. Further stabilization could result from additional π–π interactions between benzyl groups of neighboring $DBV^{\bullet+}_{(ads)}$ molecules within the 1D polymer chain. It should be stressed that such an effective π–π interaction between adjacent $DBV^{\bullet+}_{(ads)}$ molecules can only be realized on the surface if the benzyl groups take up a *trans*-conformation. A further steric requirement for the stabilization of the 1D polymer chains consists in the slight lateral shift of adjacent $DBV^{\bullet+}_{(ads)}$ molecules and explains the slight deviation from an ideal face-to-face arrangement. As a consequence of that, the propagation direction of the 1D polymer chain is not exactly perpendicular to the main molecular axes of the $DBV^{\bullet+}_{(ads)}$ molecules (Fig. 14 and 15).

On Cu(100)–$c(2 \times 2)$-Cl we determine a $DBV^{\bullet+}_{(ads)}$ surface coverage of about Θ = 0.2 ML with respect to the chloride lattice or Θ = 0.1 ML with respect to the bare Cu(100)–(1×1). The area required for each $DBV^{\bullet+}_{(ads)}$ molecule on Cu(100)–$c(2 \times 2)$-Cl amounts to 0.648 nm^2.

Similar intermolecular spacings as observed on Cu(100)–$c(2 \times 2)$-Cl have recently been found for $DBV^{\bullet+}_{(ads)}$ related phases on HOPG (Fig. 17), on bromide modified Cu(100)[40] and on chloride modified Cu(111).[33] These results clearly point to structural motifs of the $DBV^{\bullet+}_{(ads)}$ phases which are largely independent of the electronic and geometric substrate properties, in stark contrast to the 2D phase behavior of $DBV^{2+}_{(ads)}$. Obviously, the intermolecular interactions are governing the surface phase behavior of the radical mono-cations.

A further change to the potential regime where peak P2 appears in the CV (Fig. 5) initiates a further slow decay of the stripe pattern phase leaving a disordered viologen phase behind (Fig. 18). Preferential centers for this structural transition are again domain boundaries within the stripe pattern. Also this process is quasi-reversible (STM data are not shown here).

The basic cause for this further structural transition is still under discussion. One plausible explanation is based on the assumption of a chloride desorption through the $DBV^{\bullet+}_{(ads)}$ viologen film at these negative potentials causing the observed order–disorder transition. Such a chloride desorption changes again the delicate balance between the adsorbate–substrate and the inter-adsorbate interactions. $DBV^{\bullet+}_{(ads)}$ molecules can now directly interact with the metallic copper substrate. The reorganization of the $DBV^{\bullet+}_{(ads)}$ species to 1D oligomer or polymer chains now on top of the bare copper as indicated by the white arrows in Fig. 18e–f is much slower than on the chloride modified electrode surface.

4. Conclusions

The surface redox chemistry of adsorbed dibenzyl-viologens has been studied by means of cyclic voltammetry in combination with *in situ* STM focusing on the transition of the di-cationic $DBV^{2+}_{(ads)}$ molecules to the reduced $DBV^{\bullet+}_{(ads)}$ species. For both redox-states laterally well ordered viologen films are observed on the chloride modified Cu(100) electrode. An enhanced electrostatic interaction between the di-cationic species and the negatively charged chloride lattice is identified as the most important driving force for DBV^{2+} adsorption on Cu(100)–$c(2 \times 2)$-Cl. The subsequent lateral ordering of $DBV^{2+}_{(ads)}$ molecules is strongly affected by the substrate symmetry. Therefore, the $c(2 \times 2)$-Cl lattice can be regarded as a template for the lateral ordering of $DBV^{2+}_{(ads)}$ molecules. In contrast to that we find structural motifs within the $DBV^{\bullet+}_{(ads)}$ phase on Cu(100)–$c(2 \times 2)$-Cl that are widely independent of the structural and electronic substrate properties. Here, we observe strong intermolecular interactions and pronounced steric effects governing the phase behavior on the surface. 1D polymer chains of π-stacked $DBV^{\bullet+}_{(ads)}$ molecules order

themselves into a stripe pattern phase. The quasi-reversible transition from the $DBV^{2+}_{(ads)}$ related cavitand phase to this stripe pattern occurs *via* nucleation and growth.

Chloride desorption through the viologen layer at more negative electrode potentials causes a further structural transition from the ordered stripe pattern to a disordered viologen phase.

Acknowledgements

This work has been supported by the SFB 624 of the Deutsche Forschungsgemeinschaft (DFG) and the Daimler-Benz Foundation.

References

1 J. M. Lehn, *Supramolecular Chemistry*, VCH, Weinheim, Germany, 1st edn, 1995.
2 J.-M. Lehn, *Angew. Chem., Int. Ed. Engl.*, 1988, **27**, 89.
3 F. Vögtle, *Supramolecular Chemistry: An Introduction*, Wiley and Sons, Chichester, UK, 1st edn, 1991.
4 A. E. Kaifer and M. Gomez-Kaifer, *Supramolecular Electrochemistry*, VCH, Weinheim, Germany, 1st edn, 1999.
5 V. Balzani, M. Venturi and A. Credi, *Molecular Devices and Machines*, Wiley-VCH, 1st edn, 2003.
6 S. De Feyter and F. C. De Schryver, *Chem. Soc. Rev.*, 2003, **32**, 139.
7 C. L. Bird and A. T. Kuhn, *Chem. Soc. Rev.*, 1981, **10**, 49.
8 P. M. S. Monk, *The Viologens: physicochemical properties, synthesis and applications of the salts of 4,4′-bipyridines*, John Wiley and Sons Ltd., Chichester, UK, 1st edn, 1998.
9 K. Kobayashi, F. Fujisaki, T. Yoshimina and K. Nik, *Bull. Chem. Soc. Jpn.*, 1986, **59**, 3715.
10 K. Arihara, T. Ohsaka and F. Kitamura, *Phys. Chem. Chem. Phys.*, 2002, **4**, 1002.
11 T. Lu and T. M. Cotton, *J. Phys. Chem.*, 1987, **91**, 5978.
12 T. Lu, T. M. Cotton, J. K. Hurst and D. H. P. Thompson, *J. Phys. Chem.*, 1988, **92**, 6978.
13 S. H. Shen and X. M. Ren, *Spectrochim. Acta*, 1996, **51A**, 717.
14 X. Y. Tang, T. Schneider and D. A. Buttry, *Langmuir*, 1994, **10**, 2235.
15 X. Y. Tang, T. Schneider, J. W. Walker and D. A. Buttry, *Langmuir*, 1996, **12**, 5921.
16 P. Crouigneau, O. Enea and B. Beden, *J. Electroanal. Chem.*, 1987, **218**, 307.
17 P. Crouigneau, B. Beden, A. M. Braun and O. Enea, *J. Electroanal. Chem.*, 1987, **234**, 329.
18 F. Kitamura, T. Ohsaka and K. Tokuda, *J. Electroanal. Chem.*, 1993, **353**, 323.
19 K. Arihara, F. Kitamura, T. Ohsaka and K. Tokuda, *J. Electroanal. Chem.*, 1999, **488**, 138.
20 K. Arihara, F. Kitamura, K. Nukanobu, T. Ohsaka and K. Tokuda, *J. Electroanal. Chem.*, 2000, **473**, 117.
21 T. Sagara and K. Miuchi, *J. Electroanal. Chem.*, 2004, **567**, 193.
22 M. Wilms, M. Kruft, G. Bermes and K. Wandelt, *Rev. Sci. Instrum.*, 1999, **70**(7), 3641.
23 P. Broekmann, M. Wilms, M. Kruft, C. Stuhlmann and K. Wandelt, *J. Electroanal. Chem.*, 1999, **467**, 307.
24 S. Huemann, H. Zajonz, H. Dosch, P. Broekmann and K. Wandelt, *J. Phys. Chem. B*, submitted.
25 D. W. Suggs and A. J. Bard, *J. Phys. Chem. B*, 1995, **99**, 8349.
26 M. R. Vogt, A. Lachenwitzer, O. M. Magnussen and R. J. Behm, *Surf. Sci.*, 1998, **399**, 49.
27 O. M. Magnussen, *Chem. Rev.*, 2002, **102**, 679.
28 M. T. M. Koper, *J. Electroanal. Chem.*, 1998, **450**, 189.
29 M. Kunitake, N. Batina and K. Itaya, *Langmuir*, 1995, **11**, 2337.
30 K. Ogaki, N. Batina, M. Kunitake and K. Itaya, *J. Phys. Chem.*, 1996, **100**, 7185.
31 N. Batina, M. Kunitake and K. Itaya, *J. Electroanal. Chem.*, 1996, **405**, 245.
32 S. Kossmann, P. Broekmann and B. Kirchner, unpublished work.
33 D. T. Pham, K. Wandelt and P. Broekmann, unpublished work.
34 C. Safarowsky, K. Wandelt and P. Broekmann, *Langmuir*, 2004, **20**, 8261.
35 C. Safarowsky, A. Rang, C. A. Schalley, K. Wandelt and P. Broekmann, *Electrochim. Acta*, 2005, **50**, 4257.
36 P. Broekmann, M. Anastasescu, A. Spaenig, W. Lisowski and K. Wandelt, *J. Electroanal. Chem.*, 2001, **500**, 241.
37 M. J. Blandamer, J. A. Brivati, M. F. Fox, M. C. R. Symons and G. S. P. Verma, *Trans. Faraday Soc.*, 1967, **63**, 1850.
38 F. M. Hawkridge, H. L. Landrum and R. T. Salmon, *J. Am. Chem. Soc.*, 1977, **99**, 3154.
39 M. Hawkridge, J. F. Stargardt, H. L. Landrum and R. T. Salmon, *Anal. Chem.*, 1978, **50**, 930.
40 K. Gentz, K. Wandelt and P. Broekmann, unpublished work.